The ıQuad sensor: a new Fourier-based wave front sensor derived from the 4 quadrants coronagraph

Olivier Fauvarque, Victoria Hutterer, Pierre Janin-Potiron, Julien Duboisset, Carlos Correia, Benoit Neichel, Jean-Francois Sauvage, Thierry Fusco, Iuliia Shatokhina, Ronny Ramlau, et al.

The 𝔷Quad sensor: a new Fourier-based wave front sensor derived from the 4 quadrants coronagraph

Olivier Fauvarque[1,2,*], **Victoria Hutterer**[3], **Pierre Janin-Potiron**[1,4], **Julien Duboisset**[2], **Carlos Correia**[1], **Benoit Neichel**[1], **Jean-Francois Sauvage**[1,4], **Thierry Fusco**[1,4], **Iuliia Shatokhina**[5], **Ronny Ramlau**[3,5], **Vincent Chambouleyron**[1,4], **Yoann Brûlé**[1]

[1]Aix Marseille Univ, CNRS, CNES, LAM, Marseille, France
[2]Aix-Marseille Univ, CNRS, Institut Fresnel, Marseille, France
[3]Industrial Mathematics Institute, Johannes Kepler University Linz, Altenbergerstrasse 69, 4040 Linz, Austria
[4]ONERA–the French Aerospace Laboratory, F-92322 Chatillon, France
[5]Johann Radon Institute for Computational and Applied Mathematics, Linz, Austria
[*]Corresponding author: olivier.fauvarque@lam.fr

Abstract. Some coronagraph masks can be turned into wave front sensing masks thanks to minor modification. For instance, one only has to divide by two the depth of the central well to convert the Roddier & Roddier coronograph into the Zernike wave front sensor (WFS). Physically, the opposition of phase in coronagrapy becomes a quadrature phase in wave front sensing. Here, we replicate this idea to the Four Quadrant Phase Mask (FQPM) coronagraph by introducing a sensor that we call the 𝔷Quad WFS, generated by a mask which has the same geometrical structure as the FQPM but with a modified differential piston. An optical and mathematical description of this new WFS is firstly provided showing its great elegance and the central role played by the Hilbert transform in its understanding. We then compare its performance criteria with two classical wave front sensors. We finally show the 𝔷Quad sensor has major similarities to the Pyramid sensor making it a wonderful theoretical object to improve our understanding of this sensor.

1 Introduction

Fourier-based Wave front sensors[1] and coronagraphs both use optical Fourier filtering. Such a technique allows, thanks to a mask placed in a focal plane, to handle the light in its spatial frequencies space (Fig. 1). In coronagraphy, these masks are designed to reject light while in wave front sensing they are built to convert phase fluctuations into intensity fluctuations. Some coronagraph masks may be turned into wave front sensing masks by minor modification. For

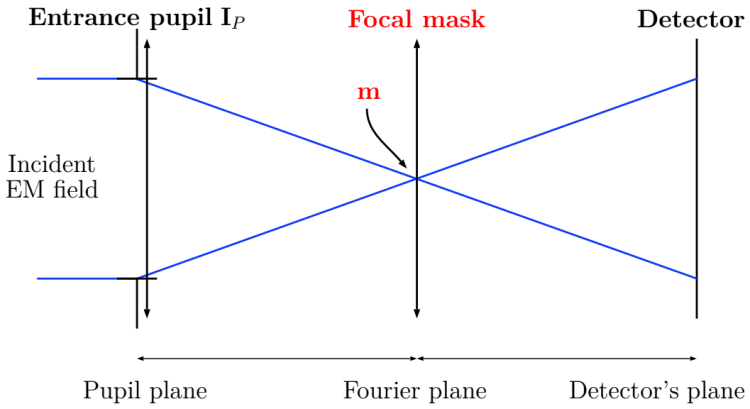

Fig 1 Schematic view (in 1D) of a Fourier filtering optical system.

instance, the Roddier & Roddier coronagraph[2] and the Zernike WFS[3,4] both use a mask which has a small circular well in its midst. For an optical system working at the wavelength λ, the depth of this well equals to $\lambda/2$ in the coronagraph configuration while it is $\lambda/4$ for the Zernike sensor. Physically, the depth $\lambda/2$ implies a π phase shift between the fields inside and outside the central well: they are in opposition of phase. This fact induces the *destructive* interference which are required in coronagraphy. For the Zernike WFS, the phase shift equals to $\pi/2$; fields are now in phase quadrature.

2 The four quadrants wave front sensors class

We propose here to extent this idea to another coronagraph called the Four Quadrants Phase Mask.[5] Its mask has a cartesian structure: the focal (or Fourier) plane is divided into 4-quadrants around the origin. In the coronagraph configuration, each quadrant is π phase-shifted with its two neighbors (left insert of Fig. 2). We introduce in this paper a class of masks which have the same geometrical structure but with a shift not equal to π; namely, their differential

piston δ will have an arbitrary value between $-\lambda/2$ and $\lambda/2$ (right insert of Fig. 2). The purpose of this article is to study the mathematical properties of these new optical objects and to examine their performance criteria in a wave front sensing context.

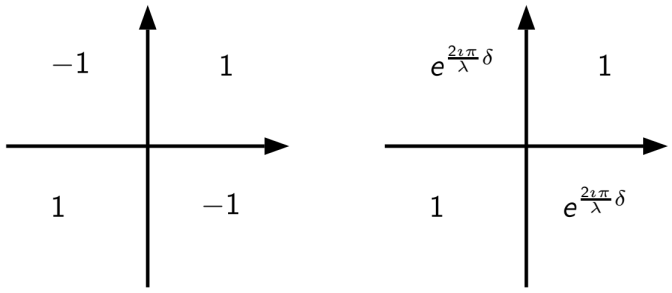

Fig 2 Transparency functions of the coronograph FQPM (left) and its generalization to an arbitrary differential piston δ (right).

The propagation through an optical Fourier filtering system using a four quadrants mask with an arbitrary differential piston can be described by a linear operator $\mathcal{W}$ which gives the electric field in the detector plane depending on the incident electric field

$$\mathcal{W} = e^{\frac{\imath\pi}{\lambda}\delta}\left[\cos\left(\frac{\pi\delta}{\lambda}\right)\mathcal{I} + \imath\sin\left(\frac{\pi\delta}{\lambda}\right)\mathcal{H}\right]. \tag{1}$$

Here $\mathcal{I}$ represents the identity operator[1] and $\mathcal{H}$ the 2D Hilbert transform along x and y axis

$$\mathcal{H}[f](x,y) = \frac{1}{\pi^2}\, p.v. \int_{\mathbf{R}^2} \mathrm{d}x'\mathrm{d}y' \frac{f(x',y')}{(x-x')(y-y')}, \tag{2}$$

where $p.v.$ indicates the principal value meaning. It is worth noticing that this operator is involutive and conserves the energy, i.e., the $\mathcal{L}^2$-norm. We observe that the field operator $\mathcal{W}$ in Eq. (1) contains two terms, the first one reproduces the incoming field while the second one provides its 2D Hilbert transform. The differential piston δ acts as a cursor between the two contributions. For $\delta = 0$ the masks are pointless since the propagator operator only contains the identity operator. The coronagraph case $\delta = \lambda/2$ gives a pure 2D Hilbert transform. Finally, if $\delta = \pm\lambda/4$, there is a perfect energy equipartition between the two terms.

In a wave front sensing context, we write the incident field as $\mathbf{I}_P e^{\imath\phi}$ where $\mathbf{I}_P$ is the indicator function of the entrance pupil and ϕ the phase-to-be-measured. For the sake of simplicity, the flux is considered unitary. The detector intensity $I(\phi)$ equals to the square modulus of the field in the detector plane

$$\begin{aligned} I(\phi) &= \left|\mathcal{W}\left[\mathbf{I}_P e^{\imath\phi}\right]\right|^2 & (3)\\ &= \sin\left(\frac{2\pi}{\lambda}\delta\right)\mathbf{Im}\left[(\mathbf{I}_P e^{-\imath\phi})\mathcal{H}[\mathbf{I}_P e^{\imath\phi}]\right] + \sin^2\left(\frac{\pi\delta}{\lambda}\right)\left|\mathcal{H}[\mathbf{I}_P e^{\imath\phi}]\right|^2 + \cos^2\left(\frac{\pi\delta}{\lambda}\right)\mathbf{I}_P^2. & (4)\end{aligned}$$

This intensity is crucial in two aspects. Firstly, it corresponds to the image that a phase reconstructor has to invert to estimate ϕ. Secondly, it gives the energy distribution that a Lyot's stop[6] has to filter to make the light rejection efficient for coronagraphy. Such a fact becomes clearer when looking at the detector intensity for a flat incoming wave front, i.e., when ϕ equals to 0

$$I(\phi = 0) = \cos^2\left(\frac{\pi\delta}{\lambda}\right)\mathbf{I}_P^2 + \sin^2\left(\frac{\pi\delta}{\lambda}\right)\mathcal{H}[\mathbf{I}_P]^2. \tag{5}$$

Indeed, we observe that in the coronagraph case (left insert of Fig. 3), the energy location corresponds to the 2D Hilbert transform of the pupil while the cosine term is null. It is not surprising since we know that the Hilbert transform of a function has significant values where the function highly evolves, i.e., at the edge of the pupil. This is the reason why the FQPM is effective to reject light. Note that in Adaptive Optics (AO) the term $I(0)$ is also considered as a reference intensity to which a closed AO loop will try to maintain the detector intensity as close as possible. We give on the right insert of Fig. 3 this reference intensity for the case $\delta = \lambda/4$.

[1] Actually it is not rigorously the identity but the reverse operator: for the sake of clarity, we have ignored that the whole Fourier filtering system has a magnification which equals to 1.

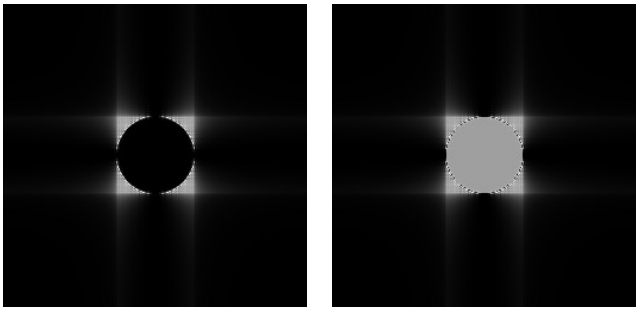

Fig 3 Intensity on the detector for a circular pupil and a null incoming phase. Left: coronagraph case $\delta = \lambda/2$. Right: energy equipartition case $\delta = \lambda/4$.

From now on, we focus on wave front sensing. We first look for the mask among the four quadrants class which optimizes the phase information coding. Then, we compare this optimal sensor to existing wave front sensors following usual AO performance criteria. First and foremost, we precise that we assume the AO control to apply linear reconstructors. In that context, finding the optimal sensor consists in maximizing the sensor sensitivity.[1] Mathematically, we therefore want to increase the ϕ-linear dependency of the intensity as much as possible. To do so, we decompose the intensity $I(\phi)$ using a Taylor's development[1] around a reference phase Φ_r which serves as the operating point of the sensor.

$$I(\phi) = I_{\text{constant}} + I_{\text{linear}}(\phi) + I_{\text{quadratic}}(\phi) + ..., \tag{6}$$

where I_{constant} equals to $I(\Phi_r)$ and does not depend on the phase ϕ. I_{linear} corresponds to the perfectly linear behavior of the sensor around the reference phase. It equals the Fréchet derivative of the intensity around Φ_r in direction ϕ (for more details see the appendix 1). $I_{\text{quadratic}}$ is the first non-linear phase-dependency. When assuming that the sensor is working around zero, i.e., $\Phi_r = 0$ we obtain

$$I_{\text{linear}}(\phi) = \sin\left(\frac{2\pi}{\lambda}\delta\right)\left[\mathcal{H}[\mathbf{I}_P]\mathbf{I}_P\phi - \mathcal{H}[\mathbf{I}_P\phi]\mathbf{I}_P\right], \tag{7}$$

$$I_{\text{quadratic}}(\phi) = \sin^2\left(\frac{\pi}{\lambda}\delta\right)\left[\mathcal{H}[\mathbf{I}_P\phi]^2 - \mathcal{H}[\mathbf{I}_P]\mathcal{H}[\mathbf{I}_P\phi]\right]. \tag{8}$$

These quantities have a similar structure: scalar terms only depending on the differential piston δ and 2D terms involving Hilbert transforms of the phase and the pupil. This pronounced decomposition is not systematic at all. The fact that the parameter δ has no influence on the spatial structure of the response to ϕ is an unexpected and very interesting characteristic of the FQPM class.

For the linear term some remarkable properties can be found. The first one is about its support. Indeed, Eq. (7) shows that it exactly corresponds to the pupil support. In other words, there is no linear information outside the pupil. Secondly, we observe that the scalar term is maximum when the differential piston ensures the energy equipartition between the real and imaginary parts of the propagation operators, i.e., $\delta = \pm\lambda/4$. Physically, this piston provides, as for the Zernike WFS, a $\pm\pi/2$ shift between the different parts of the focal plane tessellation. Such a result is in perfect agreement with the phase contrast method introduced in reference 3. Note that in the coronagraph case $\delta = \lambda/2$, the linear term is rigorously null.

The quadratic term, as all non-linear terms, is for the AO control using linear reconstructors a perturbation which has to be kept as small as possible. Its size largely determines the linearity (or dynamic) range of the sensor.[1] Unfortunately, Eq. (8) shows that this term only equals to zero for the pointless mask $\delta = 0$. In other words, it is impossible by using Fourier filtering and four quadrants masks (right insert of Fig. 2) to sense the wave front without having simultaneously a non-linear phase dependency. (Note, however, that linearity can be improved by the use of a 2 paths optical device, for more details see appendix 2.) From this discussion, we finally understand that the differential piston is also a cursor to adjust the sensitivity regarding to the linearity range of the WFS. Note, that these developments are valid for the Zernike WFS as well.

3 An optimum configuration

In what follows, we will focus on the mask with $\delta = \lambda/4$ which provides the energy equipartition. We call the associated WFS the **𝓏Quad WFS**. The notation *Quad* refers to the cartesian tessellation of the focal plane whereas the

$\imath$ emphasizes the transformation of the coronagraph FQPM transparency function (with its 1 and -1 coefficients; left insert of Fig. 2) into the $\imath$Quad WFS's one (coefficients of the right insert of Fig. 2 equal to 1 and $\imath$ if $\delta = \lambda/4$).

Let us now compare the $\imath$Quad WFS to two Fourier-based wave front sensors used in Adaptive Optics, namely the Zernike WFS[4] and the 4-sided non-modulated Pyramid WFS.[7] We precise that we assume the angle of the pyramidal prism to be large enough in order to completely separate the pupil images.

The first performance criterion is related to the number of the detector pixels required to code phase information. This aspect can be tackled in two ways. The first one is based on geometrical optics and considers that relevant phase information lies only inside pupil images. In that case, Zernike and $\imath$Quad wave front sensors need 4 times less pixels than the Pyramid WFS to reach the same amount of information which is a huge gain in terms of data to process. Note that this factor 4 is decreasing toward 1 when using a flattened Pyramid WFS,[8] i.e., a pyramid mask with a small apex angle which induces an overlap of the pupil images. The second approach is based on the study of the linear intensity. Indeed, this quantity is the main contributor for the numerical phase reconstructor to estimate the phase. As a consequence, in order to perform ultimate AO correction we want to make optimal use of sensor pixels being in the linear intensity support. We observe thanks to Eq. (7) that the intensity support itself exactly corresponds to the geometrical pupil image for the $\imath$Quad WFS. Such a fact is also true for the Zernike WFS. In contrast, it appears that there is linear information outside the 4 pupil images for the Pyramid WFS. In other words, the whole detector has to be taken into account for this sensor. Thus, the Pyramid WFS requires even *more* than 4 times the number of pixels needed to sense the wave front with a Zernike or $\imath$Quad WFS making the latter sensors efficient in terms of detector size.

We are now interested in the chromatic behavior of the $\imath$Quad. As for the coronagraph FQPM, the $\imath$Quad can be optimized for a specific wavelength only, meaning that the maximum of sensitivity will be obtained when the source's wavelength equals to the mask's optimization wavelength. Nevertheless, we observe thanks to Eq. (7) that the spatial structure of the response does not depend on the wavelength. This one has only an impact on a global scalar level. Physically, it comes from the fact that the four quadrants masks have, with their cartesian tessellation, a scale invariant geometry. It is not true for the Zernike WFS which has, due to the finite size of its central well, a spatial structure of its response changing with the wavelength. This remarkable property implies, for instance, that a calibration matrix built at a certain wavelength may be used to sense the phase with another source (or even with a polychromatic one). It will be only a matter of scalar gain. It is worth noticing that the $\imath$Quad WFS shares this property with the non-modulated Pyramid WFS.

We now study two fundamental performance criteria, namely sensitivity and linearity range and compare those for the different sensor types. The criteria are computed following the method of reference 1 and represented with respect to the Zernike polynomials in Fig. 4 and to the sine and cosine basis (i.e., the spatial frequencies) in Fig. 5

$$\text{Sine and cosine basis:} \quad \left\{ \phi^{\cos}_{\vec{\mathbf{k}}} : \vec{\mathbf{r}} \to \cos\left(2\pi\vec{\mathbf{k}}.\vec{\mathbf{r}}\right) \text{ and } \phi^{\sin}_{\vec{\mathbf{k}}} : \vec{\mathbf{r}} \to \sin\left(2\pi\vec{\mathbf{k}}.\vec{\mathbf{r}}\right) \text{ with } \vec{\mathbf{k}} \in \mathbb{R}^2 \right\}. \tag{9}$$

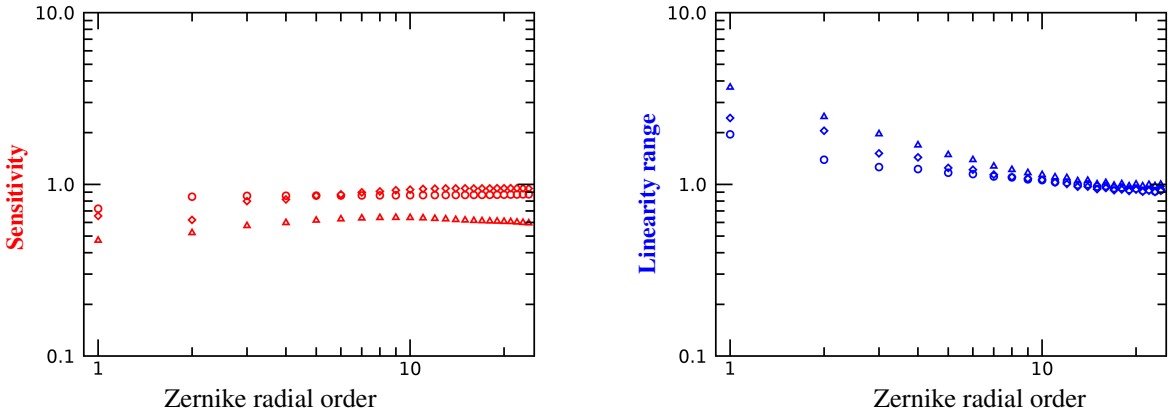

Fig 4 Sensitivity (left) and linearity range (right) with respect to the 25 first Zernike radial orders (which corresponds to around 300 Zernike polynomials). △ Pyramid. + $\imath$Quad. ○ Zernike.

In terms of linearity range (blue curves), the three wave front sensors are almost equivalent for the high frequencies. Main differences concern low frequencies, whereby the $\imath$Quad lies between the Pyramid and the Zernike performance

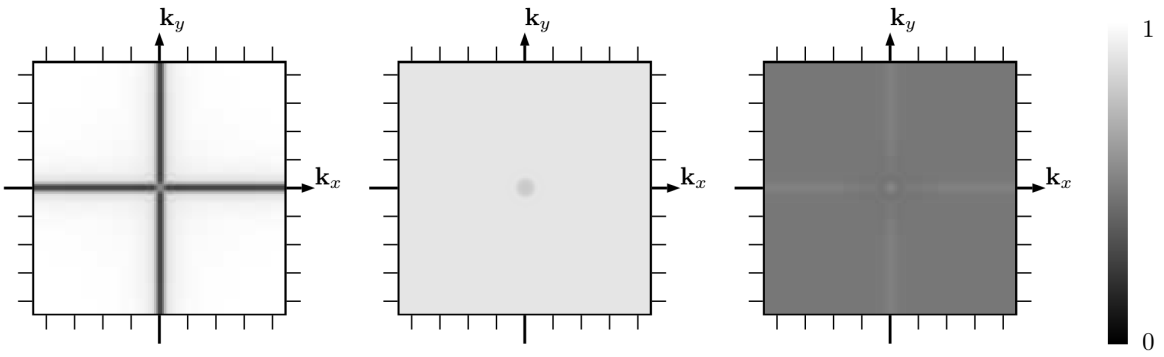

Fig 5 Sensitivity with respect to the phase spatial frequencies $\vec{\mathbf{k}} = (\mathrm{k}_x, \mathrm{k}_y)$ for the $\imath$Quad (left), Zernike (middle) and Pyramid (right) wave front sensors.

curves. Regarding the sensitivity (red curves), the $\imath$Quad surpasses the non-modulated Pyramid WFS by a factor of approximately 2 on the whole frequency range. It has similar performance as the Zernike WFS: the $\imath$Quad is slightly better for the high spatial frequencies whereas the Zernike is a bit more sensitive for the low frequencies. The largest sensitivity difference concerns the second radial order which contains the focus and the two astigmatisms aberrations. Such a reduced sensitivity is due to the fact that the $\imath$Quad sensor has difficulty to code the vertical astigmatism Z_2^2 (left insert of Fig. 6). Quantitatively, the $\imath$Quad's sensitivity with respect to this mode is almost 30 lower than the Zernike's sensitivity. The physical reason of this very low sensitivity is a matter of symmetry. Indeed, when looking at

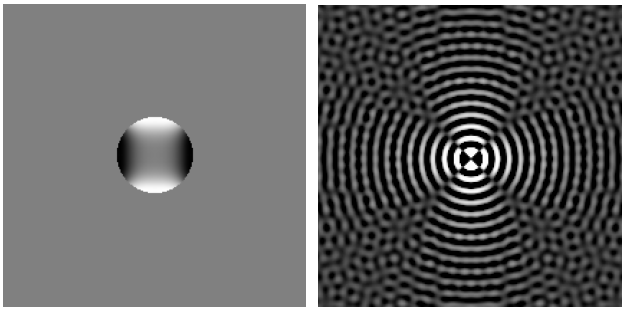

Fig 6 Left: structure of the badly-seen mode computed thanks to a singular value decomposition. Right: 2D Fourier transform of this mode.

the Fourier transform of the badly-seen mode (right insert of Fig. 6), we observe that its structure is turned through 45 degrees with respect to the $\imath$Quad mask geometry. This implies destructive interference which annihilates the linear response of the sensor to this mode. When looking at the 2D sensitivity with respect to the spatial frequencies (left insert of Fig. 5), we observe that Z_2^2 is not the only mode which is incorrectly seen by the $\imath$Quad WFS. The black cross indicates that phases which only contain pure x or y frequencies (in other words, frequencies which lie on the edge of the cartesian tessellation) are badly seen by the sensor.

Such a geometrical consideration implies that a Fourier-based WFS using a turned through 45 degrees $\imath$Quad mask is able to correctly measure the previous unseen frequencies. However, it cannot properly see the diagonals spatial frequencies. Hence, a 2-paths optical system using simultaneously two $\imath$Quad sensors with two different mask's orientations has no badly-seen spatial frequencies (see Fig. 7).

The last part of this paper is dedicated to a curious mathematical property of the $\imath$Quad WFS. Its linear intensity turns out to be very close to the slopes maps[9] of the Pyramid WFS. Slopes maps result from a numerical processing performed on the detector intensity of the Pyramid WFS. They consist in two combinations of the 4 pupil images and allow to compress the Pyramid WFS signal in two pupil images only but also to understand them in terms of phase derivatives along x and y-axis. Assuming a reflective Pyramid working in its linearity domain, the slopes maps are approximated by

$$S_x(\phi)(x,y) = \frac{\mathbf{I}_P(x,y)}{\pi} \int_P \frac{\phi(x,y) - \phi(x',y)}{x - x'} \mathrm{d}x', \tag{10}$$

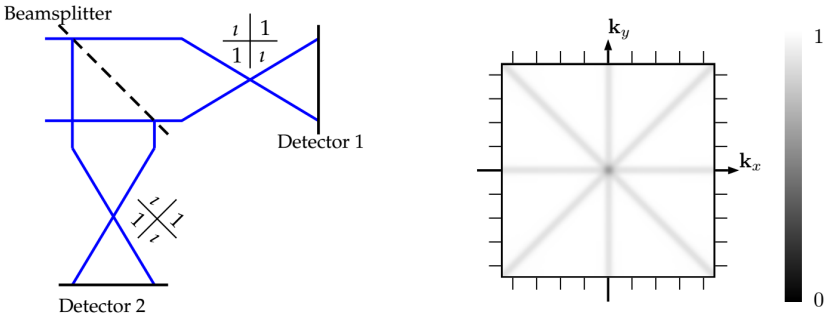

Fig 7 Left: Optical configuration of the 2-paths $\imath$Quad WFS. Right: Sensitivity with respect to the phase spatial frequencies.

$$S_y\big(\phi\big)(x,y) = \frac{\mathbf{I}_P(x,y)}{\pi}\int_P \frac{\phi(x,y)-\phi(x,y')}{y-y'}\mathrm{d}y'. \tag{11}$$

We can describe these quantities as integrated difference quotient along x and y directions. That is why slopes maps are close to the derivatives of the wave front. Nevertheless, they are not rigorously phase derivatives since the 1D Hilbert transform along x (resp. y) plays the most significant role in the S_x (resp. S_y) expression. We now compare Eqs. (10) and (11) to the linear intensity of the $\imath$Quad WFS (7). The latter becomes, if we develop it with respect to spatial coordinates,

$$I_{\text{linear}}\big(\phi\big)(x,y) = \frac{\mathbf{I}_P(x,y)}{\pi^2}\int_P \frac{\phi(x,y)-\phi(x',y')}{(x-x')(y-y')}\mathrm{d}x'\mathrm{d}y'. \tag{12}$$

Thus, it appears that the $\imath$Quad signal is a condensed version of the two Pyramid slopes maps. Indeed, this sensor optically computes in one pupil image only, the x and y Hilbert transforms of the phase. Physically, this unexpected parallel between the $\imath$Quad and the Pyramid WFS is essentially related to the fact that they both use a cartesian tessellation of the focal plane. No matter how the phase information is shaped – by doing optical interference with the differential piston of the $\imath$Quad or by splitting the spatial frequencies with prisms to then numerically processing them with the Pyramid WFS – the involved mathematical operators depend on the way we subdivide the focal plane.

The great similarity between the $\imath$Quad and Pyramid WFS slopes maps signals is profitable in many ways. Firstly, there already exist a lot of model-based reconstruction algorithms[10] dedicated to the Pyramid WFS which can be extended to build effective reconstructors for the $\imath$Quad WFS. Moreover, this numerical implementation will be facilitated by the fact that the linear intensity operator of the $\imath$Quad (12) turns out to be self-adjoint (for more details, see appendix 1); this is a very convenient property for some iterative mathematical algorithms as, e.g., the linear Landweber iteration.[10] Finally, this sensor, which is mathematically much more intelligible than the real Pyramid WFS (it does not require any assumption on the pyramid angle for instance) can be seen as a theoretical extension of the Pyramid WFS.

4 Conclusion

In this paper, we introduced a new class of Fourier-based wave front sensors derived from the FQPM coronagraph. Their filtering mask uses a cartesian tessellation of the focal plane with a unique parameter: the differential piston between quadrants. This degree of freedom allowed to find an optimal WFS regarding to the sensitivity performance, that we called the $\imath$Quad WFS. Its differential piston ensures that the fields of each neighbor quadrant are in quadrature of phase. This result proves that the shift from the coronagraph FQPM to the $\imath$Quad WFS rigorously mimics the shift from the Roddier & Roddier coronagraph to the Zernike WFS. We then studied the performance criterion of the $\imath$Quad and observed that this sensor was

- efficient in terms of the number of pixels required to sense the wave front,
- less chromatic than the Zernike WFS and
- competitive in terms of sensitivity and linearity range.

Despite the badly-seen frequencies of the $\imath$Quad, we saw that a two optical paths solution using two $\imath$Quad masks with different orientations could solve this problem. In conclusion, rather than being a practical sensor, the single

path $\imath$Quad may be viewed like a theoretical object which has an elegant mathematical formulation and also builds a bridge between the Pyramid (because of the unexpected similarity between $\imath$Quad output and the slopes maps) and the Zernike wave front sensors (since the $\imath$Quad is based on the phase contrast method).

Acknowledgments. Noah Schwartz (UK Astronomy Technology Centre, Edinburgh) is acknowledged for fruitful discussion.

Funding. Laboratoire d'Astrophysique de Marseille (LAM) (VASCO Research Project); French Aerospace Lab (ONERA); ANR-18-CE31-0018-01-WOLF; ANR Tremplin-ERC (ANR-16-TERC-0008-01); ANR A*MIDEX (ANR-11-IDEX-0001- 02); Horizon 2020 (ASHRA 730890); LABEX FOCUS; Austrian Science Fund (F68-N36, project 5); Austrian Federal Ministry of Science and Research (HRSM).

Appendices

Appendix 1: Gâteaux derivatives of the $\imath$Quad WFS

In this appendix, we prove that the Gâteaux derivative of the $\imath$Quad intensity around any reference phase Φ_r equals to

$$\begin{aligned}\big(I(\Phi_r)'\big)\phi(x,y) = \frac{\mathbf{I}_P(x,y)}{\pi^2}\int_P \mathrm{d}x'\mathrm{d}y' \frac{[\phi(x,y)-\phi(x',y')]\cos[\Phi_r(x,y)-\Phi_r(x',y')]}{(x-x')(y-y')} \\ -\frac{1}{2}\int_P\int_P \mathrm{d}x'\mathrm{d}y'\mathrm{d}x''\mathrm{d}y'' \frac{[\phi(x',y')-\phi(x'',y'')]\sin[\Phi_r(x',y')-\Phi_r(x'',y'')]}{\pi^4(x-x')(y-y')(x-x'')(y-y'')} \end{aligned} \tag{13}$$

and show that it allows to get the linear intensity I_{linear} given in Eq. (7).

Proof. We first expand the detector intensity (4) regarding to the spatial coordinates

$$\begin{aligned} I\big(\phi\big)(x,y) = \frac{\mathbf{I}_P(x,y)}{\pi^2}\int_P \mathrm{d}x'\mathrm{d}y' \frac{\sin[\phi(x,y)-\phi(x',y')]}{(x-x')(y-y')} + \\ \mathbf{I}_P^2(x,y) + \int_P\int_P \mathrm{d}x'\mathrm{d}y'\mathrm{d}x''\mathrm{d}y'' \frac{\cos[\phi(x',y')-\phi(x'',y'')]}{\pi^4(x-x')(y-y')(x-x'')(y-y'')}, \end{aligned}$$

in which it was assumed that $\delta = \lambda/4$. We may observe that this formula corresponds to a decomposition into an odd and an even part regarding to the phase: $I(\phi) = I_{\text{odd}}(\phi) + I_{\text{even}}(\phi)$ with

$$\begin{aligned} I_{\text{odd}}\big(\phi\big)(x,y) &:= \frac{\mathbf{I}_P(x,y)}{\pi^2}\int_P \mathrm{d}x'\mathrm{d}y' \frac{\sin[\phi(x,y)-\phi(x',y')]}{(x-x')(y-y')} \\ I_{\text{even}}\big(\phi\big)(x,y) &:= \frac{1}{2}\left(\mathbf{I}_P^2(x,y) + \int_P\int_P \mathrm{d}x'\mathrm{d}y'\mathrm{d}x''\mathrm{d}y'' \frac{\cos[\phi(x',y')-\phi(x'',y'')]}{\pi^4(x-x')(y-y')(x-x'')(y-y'')}\right). \end{aligned}$$

Utilizing similar to reference 11 Taylor's theorem with the Lagrange form of the remainder for the representation of sine and cosine the Gâteaux derivatives of these odd and even intensities around the reference phase Φ_r are per definition computed as

$$\begin{aligned} \left(I_{\text{odd}}(\Phi_r)'\right)\phi\,(x,y) &= \lim_{t\to 0}\frac{\left(I_{\text{odd}}\left(\Phi_r + t\phi\right)\right)(x,y) - \left(I_{\text{odd}}\left(\Phi_r\right)\right)(x,y)}{t} \\ &= \lim_{t\to 0}\frac{\mathbf{I}_P(x,y)}{\pi^2}\int_P \mathrm{d}x'\mathrm{d}y' \frac{\sin\left[\Phi_r(x,y)+t\phi(x,y)-\Phi_r(x',y')-t\phi(x',y')\right]-\sin\left[\Phi_r(x,y)-\Phi_r(x',y')\right]}{t(x-x')(y-y')} \\ &= \lim_{t\to 0}\frac{\mathbf{I}_P(x,y)}{\pi^2}\int_P \mathrm{d}x'\mathrm{d}y' \frac{\sin'\left[\Phi_r(x,y)-\Phi_r(x',y')\right]\left[t\phi(x,y)-t\phi(x',y')\right]+\mathcal{O}\left(t^2\phi^2\right)}{t(x-x')(y-y')} \\ &= \frac{\mathbf{I}_P(x,y)}{\pi^2}\int_P \mathrm{d}x'\mathrm{d}y' \frac{\left[\phi(x,y)-\phi(x',y')\right]\cos\left[\Phi_r(x,y)-\Phi_r(x',y')\right]}{(x-x')(y-y')}, \end{aligned}$$

$$
\begin{aligned}
\left(I_{\text{even}}(\Phi_r)'\right)\phi\,(x,y) &= \lim_{t\to 0}\frac{\left(I_{\text{even}}\left(\Phi_r+t\phi\right)\right)(x,y)-\left(I_{\text{even}}\left(\Phi_r\right)\right)(x,y)}{t}\\
&= \lim_{t\to 0}\frac{1}{2}\left(\mathbf{I}_P^2(x,y)+\int_P\int_P \mathrm{d}x'\mathrm{d}y'\mathrm{d}x''\mathrm{d}y''\frac{\cos\left[\Phi_r(x',y')+t\phi(x',y')-\Phi_r(x'',y'')-t\phi(x'',y'')\right]}{t\pi^4(x-x')(y-y')(x-x'')(y-y'')}\right)\\
&- \frac{1}{2}\left(\mathbf{I}_P^2(x,y)+\int_P\int_P \mathrm{d}x'\mathrm{d}y'\mathrm{d}x''\mathrm{d}y''\frac{\cos\left[\Phi_r(x',y')-\Phi_r(x'',y'')\right]}{t\pi^4(x-x')(y-y')(x-x'')(y-y'')}\right)\\
&= \lim_{t\to 0}\frac{1}{2}\int_P\int_P \mathrm{d}x'\mathrm{d}y'\mathrm{d}x''\mathrm{d}y''\frac{\cos'\left[\Phi_r(x',y')-\Phi_r(x'',y'')\right]\left[t\phi(x',y')-t\phi(x'',y'')\right]+\mathcal{O}\left(t^2\phi^2\right)}{t\pi^4(x-x')(y-y')(x-x'')(y-y'')}\\
&= -\frac{1}{2}\int_P\int_P \mathrm{d}x'\mathrm{d}y'\mathrm{d}x''\mathrm{d}y''\frac{\left[\phi(x',y')-\phi(x'',y'')\right]\sin\left[\Phi_r(x',y')-\Phi_r(x'',y'')\right]}{\pi^4(x-x')(y-y')(x-x'')(y-y'')}.
\end{aligned}
$$

The claim follows with $\boldsymbol{I}=I_{\text{odd}}+I_{\text{even}}$. □

Similar to reference 11 one can show that the Gâteaux derivative of the ıQuad sensor equals the Fréchet derivative. Note that assuming Φ_r is the null phase in Eq. (13) allows then to get the ıQuad linear intensity (12).

We are now interested in the **adjoint of the Fréchet derivative** which is a pivotal quantity in many iterative algorithms used to reconstruct the phase.[10] The $\mathcal{L}_2\left(\mathbf{R}^2\right)$-adjoint operator $\left(\boldsymbol{I}(\Phi_r)'\right)^*:\mathcal{L}_2\left(\mathbf{R}^2\right)\to\mathcal{L}_2\left(\mathbf{R}^2\right)$ of the ıQuad sensor Fréchet derivative in Φ_r is represented by

$$
\begin{aligned}
\left(I(\Phi_r)'\right)^*\phi\,(x,y) &= \frac{\mathbf{I}_P(x,y)}{\pi^2}\int_P \mathrm{d}x'\mathrm{d}y'\frac{\left[\phi(x,y)-\phi(x',y')\right]\cos\left[\Phi_r(x,y)-\Phi_r(x',y')\right]}{(x-x')(y-y')}\\
&- \int_P\int_P \mathrm{d}x'\mathrm{d}y'\mathrm{d}x''\mathrm{d}y''\frac{\phi(x',y')\sin\left[\Phi_r(x,y)-\Phi_r(x'',y'')\right]}{\pi^4(x-x')(y-y')(x'-x'')(y'-y'')}.
\end{aligned}
\tag{14}
$$

Proof. For the evaluation of the adjoints, we divide the Fréchet derivative into four parts by

$$
\begin{aligned}
I(\Phi_r)' &= I_{\text{odd}}(\Phi_r)' + I_{\text{even}}(\Phi_r)',\\
I'_{\text{odd}}(\Phi_r) &= I_{\text{odd},1}(\Phi_r) - I_{\text{odd},2}(\Phi_r),\\
I'_{\text{even}}(\Phi_r) &= I_{\text{even},1}(\Phi_r) - I_{\text{even},2}(\Phi_r)
\end{aligned}
$$

with

$$
\begin{aligned}
\left(I_{\text{odd},1}(\Phi_r)\right)\phi\,(x,y) &:= \frac{\mathbf{I}_P(x,y)}{\pi^2}\int_P \mathrm{d}x'\mathrm{d}y'\frac{\phi(x,y)\cos\left[\Phi_r(x,y)-\Phi_r(x',y')\right]}{(x-x')(y-y')},\\
\left(I_{\text{odd},2}(\Phi_r)\right)\phi\,(x,y) &:= \frac{\mathbf{I}_P(x,y)}{\pi^2}\int_P \mathrm{d}x'\mathrm{d}y'\frac{\phi(x',y')\cos\left[\Phi_r(x,y)-\Phi_r(x',y')\right]}{(x-x')(y-y')},\\
\left(I_{\text{even},1}(\Phi_r)\right)\phi\,(x,y) &:= -\frac{1}{2}\int_P\int_P \mathrm{d}x'\mathrm{d}y'\mathrm{d}x''\mathrm{d}y''\frac{\phi(x',y')\sin\left[\Phi_r(x',y')-\Phi_r(x'',y'')\right]}{\pi^4(x-x')(y-y')(x-x'')(y-y'')},\\
\left(I_{\text{even},2}(\Phi_r)\right)\phi\,(x,y) &:= -\frac{1}{2}\int_P\int_P \mathrm{d}x'\mathrm{d}y'\mathrm{d}x''\mathrm{d}y''\frac{\phi(x'',y'')\sin\left[\Phi_r(x',y')-\Phi_r(x'',y'')\right]}{\pi^4(x-x')(y-y')(x-x'')(y-y'')}.
\end{aligned}
$$

For $\phi,\psi\in\mathcal{L}_2\left(\mathbf{R}^2\right)$ with support on the telescope pupil P we consider

$$
\begin{aligned}
\left\langle\left(I_{\text{odd},1}(\Phi_r)\right)\phi,\psi\right\rangle_{\mathcal{L}_2(\mathbf{R}^2)} &= \left\langle\left(I_{\text{odd},1}(\Phi_r)\right)\phi,\psi\right\rangle_{\mathcal{L}_2(P)}\\
&= \int_P \mathrm{d}x\mathrm{d}y\left[\frac{\mathbf{I}_P(x,y)}{\pi^2}\int_P \mathrm{d}x'\mathrm{d}y'\frac{\phi(x,y)\cos\left[\Phi_r(x,y)-\Phi_r(x',y')\right]}{(x-x')(y-y')}\right]\psi\,(x,y)\\
&= \int_P \mathrm{d}x\mathrm{d}y\,\phi\,(x,y)\,\frac{1}{\pi^2}\int_P \mathrm{d}x'\mathrm{d}y'\frac{\psi(x,y)\cos\left[\Phi_r(x,y)-\Phi_r(x',y')\right]}{(x-x')(y-y')}\\
&= \left\langle\phi,\left(I_{\text{odd},1}(\Phi_r)\right)^*\psi\right\rangle_{\mathcal{L}_2(P)}\\
&= \left\langle\phi,\left(I_{\text{odd},1}(\Phi_r)\right)^*\psi\right\rangle_{\mathcal{L}_2(\mathbf{R}^2)},
\end{aligned}
$$

which results in

$$
\left(\left(I_{\text{odd},1}(\Phi_r)\right)^*\psi\right)(x,y) = \frac{\mathbf{I}_P(x,y)}{\pi^2}\int_P \mathrm{d}x'\mathrm{d}y'\frac{\psi(x,y)\cos\left[\Phi_r(x,y)-\Phi_r(x',y')\right]}{(x-x')(y-y')},
$$

i.e., $I_{\text{odd},1}$ is self-adjoint. Moreover,

$$\begin{aligned}
\left\langle \left(I_{\text{odd},2}(\Phi_r)\right)\phi,\psi\right\rangle_{\mathcal{L}_2(\mathbf{R}^2)} &= \left\langle \left(I_{\text{odd},2}(\Phi_r)\right)\phi,\psi\right\rangle_{\mathcal{L}_2(P)} \\
&= \int_P \mathrm{d}x\mathrm{d}y \left[\frac{\mathbf{I}_P(x,y)}{\pi^2}\int_P \mathrm{d}x'\mathrm{d}y' \frac{\phi(x',y')\cos\left[\Phi_r(x,y)-\Phi_r(x',y')\right]}{(x-x')(y-y')}\right]\psi\left(x,y\right) \\
&= \int_P \mathrm{d}x'\mathrm{d}y'\,\phi\left(x',y'\right)\frac{1}{\pi^2}\int_P \mathrm{d}x\mathrm{d}y \frac{\psi(x,y)\cos\left[\Phi_r(x,y)-\Phi_r(x',y')\right]}{(x-x')(y-y')} \\
&= \int_P \mathrm{d}x\mathrm{d}y\,\phi\left(x,y\right)\frac{1}{\pi^2}\int_P \mathrm{d}x'\mathrm{d}y' \frac{\psi(x',y')\cos\left[\Phi_r(x,y)-\Phi_r(x',y')\right]}{(x'-x)(y'-y)} \\
&= \left\langle \phi,\left(I_{\text{odd},2}(\Phi_r)\right)^*\psi\right\rangle_{\mathcal{L}_2(P)} \\
&= \left\langle \phi,\left(I_{\text{odd},2}(\Phi_r)\right)^*\psi\right\rangle_{\mathcal{L}_2(\mathbf{R}^2)}
\end{aligned}$$

with (as cosine is even)

$$\left(\left(I_{\text{odd},2}(\Phi_r)\right)^*\psi\right)(x,y) = \frac{\mathbf{I}_P(x,y)}{\pi^2}\int_P \mathrm{d}x'\mathrm{d}y' \frac{\psi(x',y')\cos\left[\Phi_r(x,y)-\Phi_r(x',y')\right]}{(x-x')(y-y')},$$

i.e., $I_{\text{odd},2}$ is self-adjoint as well. Similarly, for $I_{\text{even}}\left(\Phi_r\right)'$ we calculate

$$\begin{aligned}
\left\langle \left(I_{\text{even},1}(\Phi_r)\right)\phi,\psi\right\rangle_{\mathcal{L}_2(\mathbf{R}^2)} &= \left\langle \left(I_{\text{even},1}(\Phi_r)\right)\phi,\psi\right\rangle_{\mathcal{L}_2(P)} \\
&= -\int_P \mathrm{d}x\mathrm{d}y \left[\frac{1}{2}\int_P\int_P \mathrm{d}x'\mathrm{d}y'\mathrm{d}x''\mathrm{d}y'' \frac{\phi(x',y')\sin\left[\Phi_r(x',y')-\Phi_r(x'',y'')\right]}{\pi^4(x-x')(y-y')(x-x'')(y-y'')}\right]\psi\left(x,y\right) \\
&= -\int_P \mathrm{d}x'\mathrm{d}y'\phi\left(x',y'\right)\frac{1}{2}\int_P\int_P \mathrm{d}x\mathrm{d}y\mathrm{d}x''\mathrm{d}y'' \frac{\psi(x,y)\sin\left[\Phi_r(x',y')-\Phi_r(x'',y'')\right]}{\pi^4(x-x')(y-y')(x-x'')(y-y'')} \\
&= -\int_P \mathrm{d}x\mathrm{d}y\,\phi\left(x,y\right)\frac{1}{2}\int_P\int_P \mathrm{d}x'\mathrm{d}y'\mathrm{d}x''\mathrm{d}y'' \frac{\psi(x',y')\sin\left[\Phi_r(x,y)-\Phi_r(x'',y'')\right]}{\pi^4(x'-x)(y'-y)(x'-x'')(y'-y'')} \\
&= \left\langle \phi,\left(I_{\text{even},1}(\Phi_r)\right)^*\psi\right\rangle_{\mathcal{L}_2(P)} \\
&= \left\langle \phi,\left(I_{\text{even},1}(\Phi_r)\right)^*\psi\right\rangle_{\mathcal{L}_2(\mathbf{R}^2)}
\end{aligned}$$

with

$$\left(\left(I_{\text{even},1}(\Phi_r)\right)^*\psi\right)(x,y) = -\frac{1}{2}\int_P\int_P \mathrm{d}x'\mathrm{d}y'\mathrm{d}x''\mathrm{d}y'' \frac{\psi(x',y')\sin\left[\Phi_r(x,y)-\Phi_r(x'',y'')\right]}{\pi^4(x-x')(y-y')(x'-x'')(y'-y'')}$$

and

$$\begin{aligned}
\left\langle \left(I_{\text{even},2}(\Phi_r)\right)\phi,\psi\right\rangle_{\mathcal{L}_2(\mathbf{R}^2)} &= \left\langle \left(I_{\text{even},2}(\Phi_r)\right)\phi,\psi\right\rangle_{\mathcal{L}_2(P)} \\
&= -\int_P \mathrm{d}x\mathrm{d}y \left[\frac{1}{2}\int_P\int_P \mathrm{d}x'\mathrm{d}y'\mathrm{d}x''\mathrm{d}y'' \frac{\phi(x'',y'')\sin\left[\Phi_r(x',y')-\Phi_r(x'',y'')\right]}{\pi^4(x-x')(y-y')(x-x'')(y-y'')}\right]\psi\left(x,y\right) \\
&= -\int_P \mathrm{d}x''\mathrm{d}y''\,\phi\left(x'',y''\right)\frac{1}{2}\int_P\int_P \mathrm{d}x'\mathrm{d}y'\mathrm{d}x\mathrm{d}y \frac{\psi(x,y)\sin\left[\Phi_r(x',y')-\Phi_r(x'',y'')\right]}{\pi^4(x-x')(y-y')(x-x'')(y-y'')} \\
&= -\int_P \mathrm{d}x\mathrm{d}y\,\phi\left(x,y\right)\frac{1}{2}\int_P\int_P \mathrm{d}x'\mathrm{d}y'\mathrm{d}x''\mathrm{d}y'' \frac{\psi(x'',y'')\sin\left[\Phi_r(x',y')-\Phi_r(x,y)\right]}{\pi^4(x''-x')(y''-y')(x''-x)(y''-y)} \\
&= \left\langle \phi,\left(I_{\text{even},2}(\Phi_r)\right)^*\psi\right\rangle_{\mathcal{L}_2(P)} \\
&= \left\langle \phi,\left(I_{\text{even},2}(\Phi_r)\right)^*\psi\right\rangle_{\mathcal{L}_2(\mathbf{R}^2)},
\end{aligned}$$

which results in

$$\begin{aligned}
\left(\left(I_{\text{even},2}(\Phi_r)\right)^*\psi\right)(x,y) &= -\frac{1}{2}\int_P\int_P \mathrm{d}x'\mathrm{d}y'\mathrm{d}x''\mathrm{d}y'' \frac{\psi(x'',y'')\sin\left[\Phi_r(x',y')-\Phi_r(x,y)\right]}{\pi^4(x-x'')(y-y'')(x'-x'')(y'-y'')} \\
&= -\frac{1}{2}\int_P\int_P \mathrm{d}x'\mathrm{d}y'\mathrm{d}x''\mathrm{d}y'' \frac{\psi(x',y')\sin\left[\Phi_r(x'',y'')-\Phi_r(x,y)\right]}{\pi^4(x-x')(y-y')(x'-x'')(y'-y'')} \\
&= \frac{1}{2}\int_P\int_P \mathrm{d}x'\mathrm{d}y'\mathrm{d}x''\mathrm{d}y'' \frac{\psi(x',y')\sin\left[\Phi_r(x,y)-\Phi_r(x'',y'')\right]}{\pi^4(x-x')(y-y')(x'-x'')(y'-y'')}.
\end{aligned}$$

Hence, the adjoint of the Fréchet derivative of the $\imath$Quad sensor is given by

$$\begin{aligned}\left(I(\Phi_r)'\right)^* \phi(x,y) &= \left(I_{\text{odd},1}(\Phi_r)\right)^* \phi(x,y) - \left(I_{\text{odd},2}(\Phi_r)\right)^* \phi(x,y) + \left(I_{\text{even},1}(\Phi_r)\right)^* \phi(x,y) - \left(I_{\text{even},2}(\Phi_r)\right)^* \phi(x,y)\\
&= \frac{\mathbf{I}_P(x,y)}{\pi^2} \int_P \mathrm{d}x'\mathrm{d}y' \frac{[\phi(x,y)-\phi(x',y')]\cos\left[\Phi_r(x,y)-\Phi_r(x',y')\right]}{(x-x')(y-y')}\\
&- \frac{1}{2}\int_P\int_P \mathrm{d}x'\mathrm{d}y'\mathrm{d}x''\mathrm{d}y'' \frac{\phi(x',y')\sin\left[\Phi_r(x,y)-\Phi_r(x'',y'')\right]}{\pi^4(x-x')(y-y')(x'-x'')(y'-y'')}\\
&- \frac{1}{2}\int_P\int_P \mathrm{d}x'\mathrm{d}y'\mathrm{d}x''\mathrm{d}y'' \frac{\phi(x',y')\sin\left[\Phi_r(x,y)-\Phi_r(x'',y'')\right]}{\pi^4(x-x')(y-y')(x'-x'')(y'-y'')}\\
&= \frac{\mathbf{I}_P(x,y)}{\pi^2} \int_P \mathrm{d}x'\mathrm{d}y' \frac{[\phi(x,y)-\phi(x',y')]\cos\left[\Phi_r(x,y)-\Phi_r(x',y')\right]}{(x-x')(y-y')}\\
&- \int_P\int_P \mathrm{d}x'\mathrm{d}y'\mathrm{d}x''\mathrm{d}y'' \frac{\phi(x',y')\sin\left[\Phi_r(x,y)-\Phi_r(x'',y'')\right]}{\pi^4(x-x')(y-y')(x'-x'')(y'-y'')},\end{aligned}$$

which proofs the claim. □

Eq. (14) allows then to calculate the adjoint operator of the linear intensity around the null phase $\Phi_r = 0$. We get that the adjoint operator $(I_{\text{linear}})^* : \mathcal{L}_2\left(\mathbf{R}^2\right) \to \mathcal{L}_2\left(\mathbf{R}^2\right)$ of the linear $\imath$Quad sensor around the zero phase is represented by

$$(I_{\text{linear}})^*\,\phi(x,y) = \left(I(0)'\right)^*\phi(x,y) = \frac{\mathbf{I}_P(x,y)}{\pi^2}\int_P \mathrm{d}x'\mathrm{d}y' \frac{\phi(x,y)-\phi(x',y')}{(x-x')(y-y')}, \tag{15}$$

i.e., the operator is self-adjoint because of $I_{\text{linear}} = (I_{\text{linear}})^*$ as a comparison of Eq. (12) and Eq. (15) shows. This remarkable property is unprecedented in the Fourier filtering wave front sensors world and makes the $\imath$Quad particularly appropriate to model-based phase reconstructors.

Appendix 2: Improving the linearity

In this second appendix, we show how it is possible to improve the linearity of the $\imath$Quad by using a 2-paths optical design. The idea consists in dividing the field into two fields which are Fourier filtered by two different masks: the $\imath$Quad mask and its conjugate, the $-\imath$Quad, see Fig. 8.

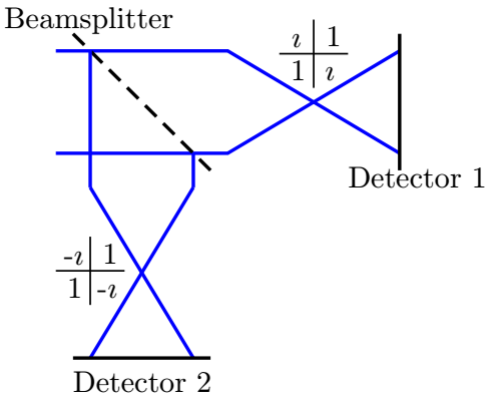

Fig 8 Optical system of the Odd $\imath$Quad.

The optical propagators of the two paths are

$$\mathcal{W}_1 = \frac{\mathcal{I} - \imath\mathcal{H}}{\sqrt{2}} \qquad \mathcal{W}_2 = \frac{\mathcal{I} + \imath\mathcal{H}}{\sqrt{2}}. \tag{16}$$

The incoming field amplitude is divided by $\sqrt{2}$ by the beamsplitter which gives two intensities:

$$I_1(\phi) = \left|\mathcal{W}_1\left[\frac{\mathbf{I}_P e^{\imath\phi}}{\sqrt{2}}\right]\right|^2 \qquad I_2(\phi) = \left|\mathcal{W}_2\left[\frac{\mathbf{I}_P e^{\imath\phi}}{\sqrt{2}}\right]\right|^2. \tag{17}$$

The WFS's output is defined as the **difference between these two intensities**:

$$dI(\phi) \quad = \quad I_1(\phi) - I_2(\phi), \tag{18}$$

which results in

$$dI\big(\phi\big)(x,y) = \frac{\mathbf{I}_P(x,y)}{\pi^2} \int_P \mathrm{d}x'\mathrm{d}y' \frac{\sin[\phi(x',y') - \phi(x,y)]}{(x-x')(y-y')} \tag{19}$$

This optical configuration allows to cancel even intensity in the $\imath$Quad intensity. In particular, the first non-linear term is the cubic one and not, as usually, the quadratic one. Such a fact implies an improvement of the sensor linearity (see Fig. 9).

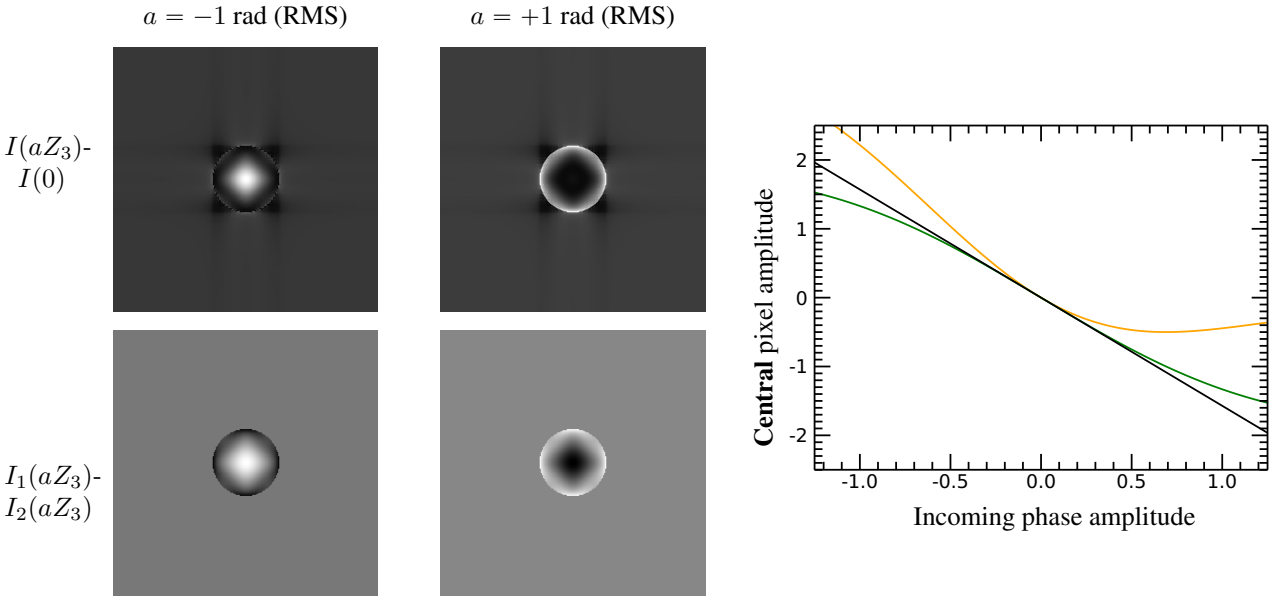

Fig 9 Left pictures: Output maps for the 1-path (top) and 2-paths (bottom) iQuad when ± 1 rad RMS Focus (Z_3) goes through the WFS. 1-path is neither odd, nor even. 2-paths is odd with respect to the phase. Moreover, it is worth noticing that there is no signal outside the pupil geometric image for the 2-paths device. Right insert: relation between the amplitude of an incoming phase and the **amplitude of the central pixel** of the WFS's output for the 1-path and the 2-paths $\imath$Quads. The same tangent at the origin indicates an identical sensitivity (black curve). Moreover, we observe that the 2-paths system provides a symmetrical response which is not the case of the 1-path. Such a fact implies a better linearity for the 2-paths $\imath$Quad than the classical one.

References

1 O. Fauvarque,"General formalism for Fourier-based wave front sensing," Optica **3**, 1440–1452 (2016).

2 F. Roddier, and C. Roddier "Stellar Coronagraph with Phase Mask," Astronomical Society of the Pacific **109**, 815–820 (1997).

3 F. Zernike, "Diffraction theory of the knife-edge test and its improved form, the phase-contrast method," Royal Astronomical Society **94**, 377–383 (1934).

4 M. N'Diaye, K. Dohlen, T. Fusco, and B. Paul, "Calibration of quasi-static aberrations in exoplanet direct-imaging instruments with a Zernike phase-mask sensor," Astronomy and Astrophysics **555**, A94 (2013).

5 D. Rouan, "The Four-Quadrant Phase-Mask Coronagraph," Astronomical Society of the Pacific **112**, 1479–1486 (2000).

6 B. Lyot, "Photographie de la couronne solaire en dehors des eclipses," Compte-rendu Academie Scientifique de Paris **193-1169**, 48 (1931).

7 R. Ragazzoni, "Pupil plane wavefront sensing with an oscillating prism," Journal of Modern Optics **43**, 289–293 (1996).

8 O. Fauvarque, B. Neichel, T. Fusco, and J.-F. Sauvage, "Variation around a pyramid theme : optical recombination and optimal use of photons," Optics Letters **15**, 3528–3531 (2015).

9 C. Vérinaud, "On the nature of the measurements provided by a pyramid wave-front sensor," Optics Communications **233**, 27–38 (2004).
10 V. Hutterer, I. Shatokhina, A. Obereder, and R. Ramlau, "Wavefront reconstruction for ELT-sized telescopes with pyramid wavefront sensors," Proc. SPIE **1070344**, (2018).
11 V. Hutterer, I. Shatokhina, and R. Ramlau, "Real-time Adaptive Optics with pyramid wavefront sensors: A theoretical analysis of the pyramid sensor model," Inverse Problems **35(4)**, 045007 (2019).